# Tuning $CO_2$ capture and conversion with Metal-Organic Frameworks crystallized in aqueous graphene oxide suspensions

*Francisco G. Cirujano*[*a], Nuria Martín[a], Elena López-Maya[b], Mayra G. Álvarez[b], M[a] Jesús Sánchez-Montero[c], Eduardo García-Verdugo[a], M[a] Dolores Merchán*[c], M[a] Mercedes Velázquez*[c]*

[a]Departamento de Química Inorgánica y Orgánica, Universidad Jaume I, Av. Sos Baynat, s/n, Castelló de la Plana, Castellón, 12071 Spain

[b] Departamento de Química Inorgánica, Universidad de Salamanca, Plaza de los caídos, s/n, 37008, Salamanca, Spain

[c] Departamento de Química Física, Universidad de Salamanca, Plaza de los caídos, s/n, 37008, Salamanca, Spain

KEYWORDS: Metal-organic frameworks, Graphene Oxide, Carbon dioxide, Adsorption, Catalysis

ABSTRACT

We present a green procedure for the synthesis of metal-organic frameworks (having either Zn, Ni and Co) in graphene oxide aqueous suspension (obtained with graphitized or non-graphitized carbon nanofibers) avoiding organic solvents and high temperatures. The materials were thoroughly characterized using XRD, SEM, $N_2$/$CO_2$-physisorption, Raman and XPS spectroscopies, and TGA. Our results demonstrate that the nature of the metal (electronegativity) and graphene oxide (oxygen-containing defects) are key in the

size, porosity and defectivity (free non-coordinated linkers and open metal sites) of the MOF and significantly affect their $CO_2$ adsorption energy (up to 6 $kJ \cdot mol^{-1}$ increase), uptake (up to 5·$mmol_{CO2} \cdot g^{-1}$ increase) and catalytic activity (up to 35% rate increase with respect to bulk MOFs) in the solvent-free ambient pressure $CO_2$ cycloaddition to epoxides.

## INTRODUCTION

The combined open metal sites in MOF 3D-nanocrystals with the high surface area and robustness of activated graphene or graphene oxide (GO) 2D-nanosheets within the material are promising combinations when aiming at gas sorption and catalysis applications, such as $CO_2$ capture and conversion strategies. Several successful approaches have been described in the literature that utilize MOFs and graphene in thermocatalytic applications. In addition, review articles have been published that focus on the synthesis, properties, and potential of these MOF-graphene systems in various catalytic processes.[1-5] These reviews highlight the advantages of combining MOFs with graphene, such as enhanced surface area, improved stability, and increased catalytic efficiency, making them promising candidates for a range of thermocatalytic applications. However, it remains a challenge to manufacture such a compound in a scalable manner and avoid the use of polluting organic solvents, which is one of the driving forces of the present work. MOF-74, prepared from divalent metals and deprotonated 2,5-dihydroxyterephthalic acid ($dot^{4-}$) linker, has a 3D framework with 1D hexagonal channels (pores) presenting a high density of open metal sites at its corners.[6] It has demonstrated potential for $CO_2$ capture due to its interaction at Lewis acid sites upon evacuation of solvent molecules, such as water.[7,8] The Zn/Co/Ni-MOF-74 coordination polymers, with their well-isolated Lewis acid sites at the metal clusters, have been used

not only as a $CO_2$ adsorbent but also as a catalytic system for the cycloaddition of $CO_2$ to epoxides. The metal centers in the MOF enhance $CO_2$ activation, enabling efficient conversion into cyclic carbonates through reaction with epoxides.[9]

The synthesis of bulk MOF-74 adsorption systems typically involves solvothermal conditions, which require large volumes of organic solvent (such as N, N'-dimethylformamide, DMF), high temperatures (above 100°C), and extended reaction times (several days). In contrast, Ni-MOF-74/graphene oxide composites have been prepared under milder conditions, using organic solvents like DMF and trimethylamine (TEA) at temperatures ranging from room temperature to 60°C, with GO content varying between 3-30 wt%. These approaches highlight the different methods used to optimize the properties and performance of MOF-74-based materials.[10] However, GO is typically prepared in water and tends to aggregate at high temperatures, especially in the presence of organic solvents. This aggregation can affect the dispersion and performance of GO in composite materials, posing a challenge during the synthesis of MOF-74/graphene oxide composites under solvothermal conditions. When graphene oxide (GO) is used in common MOF synthesis solvents like DMF, its long-term stability is compromised due to its poor solubility (1.96 $\mu g \cdot mL^{-1}$). In contrast, aqueous GO suspensions exhibit better long-term stability, aligning with its higher solubility in water (6.6 $\mu g \cdot mL^{-1}$). This difference in stability has been attributed to the similar surface tension between water (72.8 $mN \cdot m^{-1}$) and GO (~62 $mN \cdot m^{-1}$), which contrasts with the much lower surface tension of DMF (37.1 $mN \cdot m^{-1}$), leading to poor interaction and dispersion of GO in the solvent.[11]

Besides improving GO stability, room-temperature aqueous synthesis offers the possibility to extend to several metals (i.e. Zn/Co/Ni-MOF-74/ GO systems) and decrease

the costs and toxicity of expensive organic solvents (such as DMF) employed during the synthesis of these advanced materials in its bulk from (i.e. Zn-MOF-74).[12, 13] On the one hand, conventional solvothermal methods (see Scheme 1a) do not deprotonate the linker and the nucleation step is slower (favoring Ostwald ripening of nanosized crystals with defect/irregularities healing not necessarily taking place at the GO interface). This often leads to larger MOF crystals (i.e. micron-size crystals instead of "colloidal" nano-sized crystals) with less external surface area available to interact with the surface groups of GO layers. On the other hand, the MOF-GO water-based precipitation composite can be synthesized quickly at room temperature (and with a high atomic economy) since the fast deprotonation and high solubility of the deprotonated linker in the water medium increase both nucleation and growth rates. Such an increase in the concentration of ligands provides more opportunities for coordination with metal centers (which can be coordinated to surface oxygen-containing functional groups of GO stacks as depicted in Scheme 1b), allowing the growth of well-ordered crystalline structures.

Moreover, the synthesis of M-MOF-74 analogues (M = Zn, Co, and Ni) in aqueous suspensions of two types of graphene oxide (GO), each containing varying amounts of surface oxygen groups and different types of structural defects, enables the modulation of MOF crystallization. The presence of these different GO characteristics influences the growth and morphology of the MOF, allowing for the tailored design of materials with specific properties. This characteristic enhances the properties of GO, such as its reactivity and dispersion, favoring its integration into composite materials. The GO monolayers present carboxylate, epoxide and phenolate-like (i.e. upon base/water-assisted epoxide ring opening) functional groups (>10%) similar to those present at the dot linker, which may act as anchoring/coordination points of the metal to start the crystal nucleation upon coordination with the dot linker and formation of the MOF SBUs.

Working under aqueous NaOH conditions (as opposed to solvothermal methods schematized in Scheme 1a) facilities ring-opening of the epoxide with the phenolate from $dot^{4-}$ linker, as well as ionization of carboxylic acid and hydroxyl groups, generating electro-donating charged groups as an anchoring point for MOF nucleation and growth (Scheme 1b).

This work aims to not only improve the environmental sustainability of MOF-GO synthesis but also to investigate the incorporation and cooperative interactions between the porous coordination polymer and graphene oxide, as well as the impact of the GO structure on MOF crystallization. Carbon nanofibers are used instead of graphite for GO production, as they contain very few graphene layers (between 5 and 9), resulting in graphene oxides that are nearly monolayer. Additionally, a water-based MOF synthesis approach is utilized, leveraging aqueous GO suspensions to obtain the MOF-GO nanohybrids. To understand the nature of both the MOF and GO in the MOF-GO catalytic system, various characterization techniques are employed, including X-ray diffraction (XRD), Raman spectroscopy, Fourier-transform infrared (FTIR) spectroscopy, X-ray photoelectron spectroscopy (XPS), thermogravimetric analysis (TGA), scanning electron microscopy (SEM), textural characterization via $N_2$ and $CO_2$ gas adsorption, and catalytic tests, such as the $CO_2$ cycloaddition to epichlorohydrin.

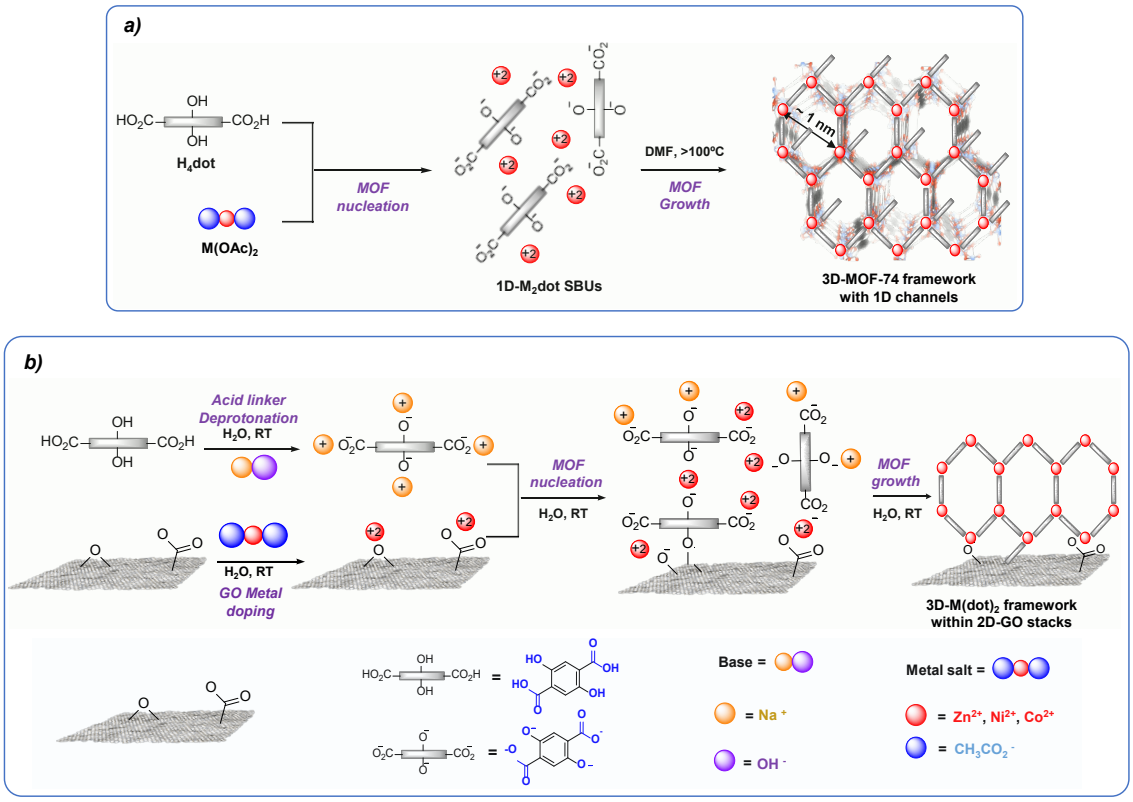


**Scheme 1.** (a) Classical solvothermal bulk 3D-MOF synthesis. (b) Merging 2D-GO with 3D-MOF nanomaterials by the room temperature aqueous MOF synthesis from GO solutions, linker ($dot^{4-}$) and metal salts (Zn, Ni, Co).

## EXPERIMENTAL SECTION

*Materials*. The reagents used for nanofiber oxidation $NaNO_3$ (99%), $H_2SO_4$ (98% w), $KMnO_4$ (>99%) and $H_2O_2$ (30% V) were supplied by Sigma Aldrich (Madrid, Spain). Carbon dioxide ($CO_2$) and nitrogen ($N_2$) of a minimum purity of 99.999 % were purchased by Air Liquide, (Madrid, Spain). Millipore Ultra-pure water was obtained by a combination of RiOs and Milli-Q systems from Millipore. The conductivity and the surface tension values of water were <0.2 $mS \cdot cm^{-1}$ and 72.5 $mN \cdot m^{-1}$, respectively.

*Structural Characterization*. The porous texture of the samples was analyzed from the adsorption isotherms of $N_2$ at -196 ºC and of $CO_2$ at 0 ºC The equipment used was

automatic Micromeritics ASAP 2010 volumetric adsorption. The adsorption of the two gases provides complementary information since $N_2$ is adsorbed into micropores larger than 0.7 nm, while the adsorption of $CO_2$ takes place in smaller micropores (<0.7 nm). Accordingly, the specific surface area was obtained from the BET equation and the $N_2$ adsorption isotherms, while the micropore volume was calculated from the Dubinin–Raduskhevic equation,[14] and the $CO_2$ adsorption isotherms.

Raman spectra were carried out at room temperature with a LabRAM HR Evolution micro-Raman spectrometer (Horiba Jobin-Yvon) using a solid-state laser operating at 532 nm and a 100× objective (laser spot size ≈ 1 $\mu m^2$). Calibration was done with the Si band centered at 520.7 $cm^{-1}$. The acquisition time was 3 s at each point to obtain the Raman spectra of the materials. The sample area was scanned with a spatial resolution of approximately 0.5 μm. The laser excitation power was kept below 1 mW to avoid laser-induced damage. Each Raman spectrum was recorded in at least four different zones and the spectra presented in the figures are averages of all these measurements. The spectral resolution of the reported spectra was 2 $cm^{-1}$. XPS measurements were performed on a SPECS spectrometer equipped with a Phoibos 150 MCD–9 analyzer using a non-monochromatic Mg KR (12536 eV) X-ray source working at 50 W. Microscopy images were obtained with a Hitachi S4800 SEM-FEG (scanning electron microscopy- field emission gun) equipment, with an accelerating voltage of 20kV, coupled with an Energy Dispersive X-ray (EDX) detector. FT-IR spectra of the cyclic carbonate of epichlorohydrin were acquired with a Pike single-reflection ATR diamond/ZnSe accessory in a JASCO FT/IR-4700 instrument. X-ray diffraction patterns were obtained with a D4 Endeavor, Bruker-AXS powder diffractometer. TGA- DSC3 Mettler Toledo coupled to a quadrupole mass spectrometer PFEIFFER VACUUM model OmniStar GSD 320 O3, 1-300 uma.

*Synthesis of graphene oxide:* The method used for the synthesis of graphene oxide was modified Hummers' method developed by our group to obtain highly oxidized GO sheets of a few layers from graphite[15] and carbon nanofibers.[16, 17] In the oxidation step, the reactive solution of $NaNO_3/H_2SO_4/KMnO_4$/graphite or carbon nanofibers was stirred at 35 ºC overnight until a thick paste was formed. This is the main difference with the Hummers' method, which spends 30 min in the oxidation stage. In the purification method also modified, the GO filter cake was dispersed in warm water and then was centrifuged at 4000 rpm for 15 min to remove the biggest (visible) particles and the supernatant was further centrifugated at 10000 rpm for 15 min to eliminate the water-soluble products of the oxidation process. In this work, the precursors were helical ribbon carbon nanofibers (graphitized and non-graphitized) ®, provided by Carbon Advanced Materials of Grupo Antolín (Burgos, Spain). These commercial nanofibers are obtained by chemical vapor deposition (CVD) using the floating catalyst method.[18] The graphene oxides thus obtained are named GO1 from carbon nanofibers graphitized and GO2 carbon nanofibers non-graphitized. The concentration of the graphene oxide solutions was determined by weighing the solid obtained after removing the solvent from a given GANF volume of each solution. The values found were 2.037 $g \cdot L^{-1}$ (GO1) and 1.553 $gL^{-1}$ (GO2).

*GO-MOF synthesis:* The synthesis of bulk MOFs and GO/MOF composites with different metals (Zn, Co, Ni) and graphene oxide (graphitized or not) contents was adapted from references 12 and 19 (see Scheme 2 and Figure S1). Briefly, two aqueous solutions were separately prepared (A and B): *(i)* Solution *A*: 30 mg of 2,5-dihydroxybenzene-1,4-dicarboxylic acid ($H_4$dot) (0.15 mmol) were dissolved in a NaOH aqueous solution, prepared from 23 mg NaOH (0.6 mmol, 4eq.) in 1 mL $H_2O$ under stirring and with the help of an ultrasonic bath. The yellow $H_4$dot linker turned into a wine color solution when deprotonated by NaOH. *(ii)* Solution *B*: ca. 75 mg of the metal acetate hydrate (2 eq. with

respect to $H_4$dot) were dissolved in 1 mL, 3 mL or 9 mL of aqueous GO solution (ca. 1 mg·mL$^{-1}$) under stirring at 200 rpm for 15 min. The MOF precipitate was formed (after a few minutes) upon dropwise addition of 1 mL of solution A to the metal-GO solutions (B), under stirring at room temperature, keeping the stirring for 24 h at room temperature. The MOFs were washed with 4 mL of water and 2 mL of methanol, recovering the solid by centrifuging at 6000 rpm, and dried at 60 ºC under vacuum during 24h. 21 MOF-GO hybrid material samples were obtained, based on the three different metals, the two different GOs and the three GO dilutions employed.

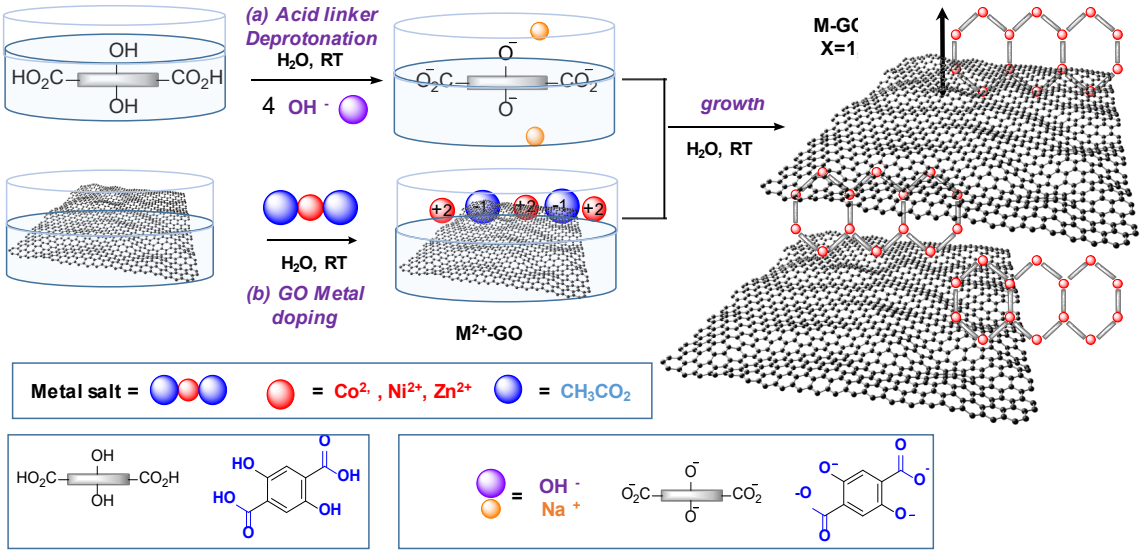


**Scheme 2.** Fast precipitation GO/MOF composite synthesis from aqueous solutions of graphene oxide (GO) with the metal acetates and ionized 2,5-dihydroxyterephthalate ($H_4$dot) under room temperature conditions. GO1 (graphitized), GO2 (non-graphitized).

## RESULTS AND DISCUSSION

On the one hand, the crystallization of targeted MOF-74 in the two GO solutions (GO1 and GO2, prepared from non-graphitized or graphitized carbon nanofibers, respectively) with different concentrations of GO (3, 10 and 30 wt% with respect to the MOF linker)

obtained was investigated (named as M-bulk, M-GO1 or 2 (3wt%), M-GO1 or 2 (10wt%), M-GO1 or 2 (30wt%), where M=Zn, Ni or Co). Water was used as the synthesis medium with metal acetates as ion sources, while metal nitrates and a 1:1 water:ethanol mixture were also tested to assess synthesis robustness. No significant changes in XRD patterns (Figure S2) or $N_2$ physisorption (Figure S3) were observed, despite the slightly higher hysteresis for the ethanol/water-based synthesis with respect to pure water. MOF-GO samples made with the water:ethanol mixture showed slightly higher BET surface areas (62 and 70 $m^2 \cdot g^{-1}$ vs. 40 and 21 $m^2 \cdot g^{-1}$ for Zn-GO1 and Zn-GO2) and pore volumes (0.12 and 0.10 $cm^3 \cdot g^{-1}$ vs. 0.07 and 0.05 $cm^3 \cdot g^{-1}$ ). However, these values remain lower than those from classical solvothermal methods (BET surface area close to 1000 $m^2 \cdot g^{-1}$). This is likely due to the rapid precipitation method used, which results in less controlled crystal growth. As a result, the materials have smaller surface areas and lower pore volumes compared to those synthesized using slower solvothermal methods, which promote more uniform crystal formation and better-developed pores. The effect of heating the synthesis at 80ºC instead of the room temperature conditions employed was also tested, but only a slight surface area increase from 237 to 281 $m^2 \cdot g^{-1}$ was found for the Ni sample (see Table S1 in the revised ESI). Moreover, the pore volume decreased from 0.48 to 0.31 $cm^3 \cdot g^{-1}$, indicating the negligible effect of temperature increase on the textural properties of the GO-MOF composite.

Raman spectroscopy is a suitable technique to detect the existence of graphene oxide in these materials, due to the presence of two characteristic G and D bands (see Figure S4 and Figure 1). Both MOF and GO are present in all the composites as indicated by the strong G (ca. 1350 $cm^{-1}$) and D (1600 $cm^{-1}$) bands from GO (see Figure S5), along with a second-order band at ~2900 $cm^{-1}$,[20, 21] and carbon-oxygen (1400-1500 $cm^{-1}$) bonds from the MOF organic linker. As GO loading increases (from 3 to 30 wt%), the intensity of

GO bands increases, while MOF bands decrease (see Figure S4). Since these bands are present in all spectra, even in the corresponding to the most GO diluted samples, ca. M-GO1 or 2 (3wt.%), we confirm the presence of graphene oxide in all composites. Raman spectroscopy was used to analyze the interaction between GOs and the MOF linker, focusing on the most diluted GO samples (3wt.%), which are relevant for $CO_2$ adsorption and catalytic activity studies. The spectra, shown in Figure 1, include those of the MOFs without GO, two graphene oxides, and their hybrid materials. The hybrid spectra display bands from both the graphene oxides and MOFs, confirming the presence of both components. Although the D, G, and G' bands of GO provide structural insights (see Figure S6), their overlap with MOF bands made full resolution difficult. Instead, the region corresponding to the C-O and O-C-O bonds in the MOF was analyzed, as it is unaffected by the GO peaks (Figure S7).

Unfortunately, the bulk MOF already exhibits bands in the same region as the D and G bands of GO, and the position of the MOF bands depends on the metal used, leading to overlap with GO bands. Additionally, the structural defects of the GO materials vary, with GO1 having a higher D' to D intensity ratio (0.145) due to vacancies, while GO2 has a lower ratio (0.076) due to $sp^3$ defects. This contributes to the band overlap between GO1 and GO2 hybrids, complicating the quantitative analysis of intensity and position changes in the hybrids. Despite this, it was possible to analyze the C-O and O-C-O bonds of the MOF part of the composite. The C-O bond shift suggests weakened metal-oxygen coordination in the MOF due to interactions with GO, especially for the more $sp^3$-defective GO2. The validity of this mechanism will be further evaluated through XRD structural characterization and $CO_2$ adsorption capacity analysis of the different materials.

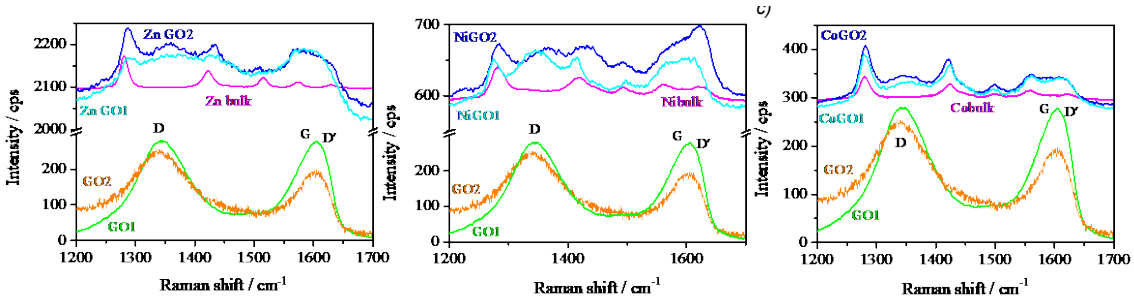


**Figure 1.** Raman spectra (region corresponding to the D/G bands of the GO component) of M=Zn (a), M=Ni (b) and M=Co (c) MOF-GO systems containing a 3wt% amount of GO1 (graphitized) or GO2 (non-graphitized).

To assess whether the green synthesis conditions used (water as solvent, room temperature) are suitable for forming the MOF-74 structure in the presence of the graphene oxide suspension (as the reaction medium), XRD analysis was performed on all samples. As shown in the diffractograms in Figure 2, all 21 samples of GO/MOF composites exhibited XRD patterns similar to those of bulk MOFs, regardless of the GO concentration, metal type, or the GO variant (GO1 and GO2). The simulated patterns for each bulk MOF are also included, along with relative changes in structural magnitudes. The similarity between the experimental and simulated XRD patterns indicates that the MOF-74 phase was successfully formed to a major extent. Two main peaks are observed, corresponding to the (110) and (300) planes at 6.7º and 11.7º, respectively. The broader peaks of Ni and Co MOF-74 (Figure 2b and c) with respect to the Zn-containing ones (Figure 2a) might be a result of their smaller crystallite size as described for other synthesis methods.[18]

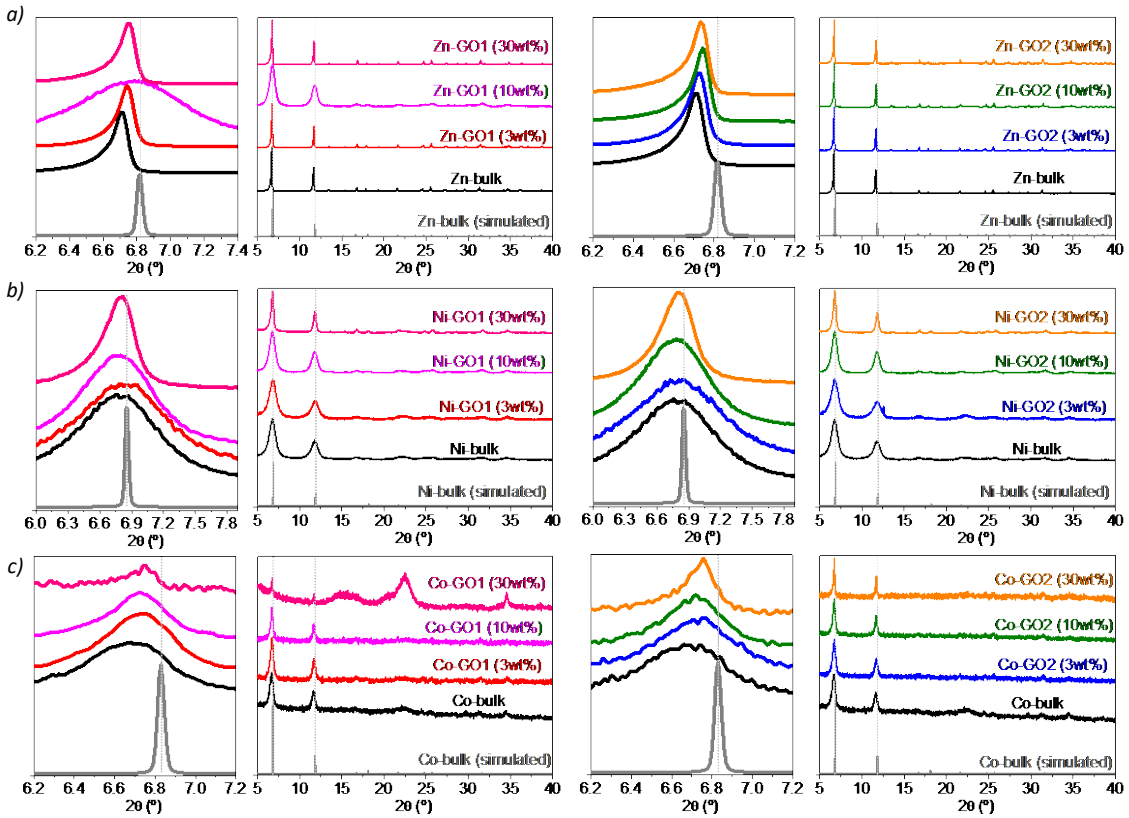


**Figure 2.** XRD patterns of Zn (a), Ni (b) and Co (c) MOF-GO1 (left) or MOF-GO2 (right) composites. GO1 (graphitized), GO2 (non-graphitized). The simulated patterns are included for comparison and the region of the most intense peak corresponding to the (110) plane is zoomed.

To study the effect of having GO within the MOF reaction medium and the nature of the GO (named GO1 and GO2) in the MOF, we have analyzed the GO-loading (3-30wt% GO with respect to the linker), also varying the GO (GO1 and GO2) and metal salt (Zn, Ni or Co acetates). The zoom of the low-angle part of the XRD for the different materials is shown in Figure 2. Both the diffraction angle (2θ) corresponding to the peak maximum and its broadness varied with the presence of GO in the synthesis medium of the MOF. On the other hand, the extra diffraction peak observed in the 2θ=10-15º region in the Co-MOF sample with higher GO loading may be attributed to GO, which appears around 12º for the (001) crystal plane, with interplanar distances of approximately 0.8 nm. This peak

nearly disappears after the reduction of GO and shifts to 25-27º, depending on the degree of reduction. The reduction can be achieved either by thermal treatment,[19] or by removing impurities from the oxidation process through alkaline treatment.[22] In our case, since the reaction is carried out in an alkaline medium, impurities are expected to have been removed, and the peak centered at 12º should not be observed. However, other studies have shown that a peak at 12-14º appears in the hydrated form of MOF-74, but not in the dehydrated form.[11, 18] Therefore, the peak around 13º in the Ni system for the sample containing GO (3 wt%) is likely due to water coordinated to the MOF, rather than GO itself (due to its low content), or the presence of dense metal oxide/hydroxide phases, which typically exhibit peaks at higher angles—these peaks are not present in this sample.

In all cases (either for Zn, Ni or Co MOFs), the diffraction angle corresponding to the most intense (110) peak is shifted to larger angles when the MOF is growth in the presence of GO (see Figure 2 and Table S1). Shifts close to 0.05º are observed for the Zn-MOF-74, while larger ones (close to 0.1º) occur for the Ni and Co-MOF-74 systems. This indicates a higher contraction of the unit cell for Ni and Co with respect to the Zn-MOF-74 when GO is present in the synthesis. While in the Zn-MOF-74, the presence of GO1 results in a slightly higher contraction of the cell with respect to GO2, in the case of either Co or Ni-MOF-74 systems, the GO2 is the one that causes a larger contraction of the framework. Although accurate calculations of unit cell parameters require a more rigorous methodology for data collection, the unit cell parameter (a) can be approximated from the Bragg equation applied to the (110) peak: $a = (\lambda/2\text{sen}\theta)(1^2+1^2+0^2)^{1/2}$, assuming a cubic cell. This is a simplified approximation, as only relative differences in the parameter will be analyzed, rather than absolute values. The relative changes in the estimated unit cell parameter (proportional to the interplanar spacing) with respect to the simulated values are plotted in Figure S8, normalized as (simulated-

experimental)/simulated. GO has minimal impact on the interplanar spacing and unit cell size, with only a slight decrease observed in the case of the cobalt system compared to the simulated MOF. No clear relationship between the changes in unit cell size and GO content is apparent.

The crystallite size of MOF nanoparticles was estimated from the full width at half maximum (FWHM) of the most intense (110) XRD peak at ca. 6.7º (see Table S2). Using the Scherrer equation (and assuming a K=0.9 and $\lambda$= 0.15418 nm),[11] the crystallite size of the MOFs found were ca. 70 nm, ca. 10 nm and ca. 20 nm for Zn-MOF-74 (Zn-bulk), Ni-MOF-74 (Ni-bulk) and Co-MOF-74 (Co-bulk), respectively. We calculated the relative decrease in crystallite size compared to the simulated XRD peak broadness (i.e., 200 nm). In Figure S8, we present the absolute difference between the experimental crystallite size of each sample and that of the simulated MOF, normalized to the simulated value, i.e. [simulated-experimental]/[simulated]. In contrast to the bulk MOFs, the presence of GO increases the crystallite size in almost all cases (compared to the simulated MOF), which correlates with the GO content, especially in the Ni and Co MOF-GO systems. This trend suggests that GO promotes MOF nucleation and growth. This behavior may be attributed to the higher density of COOH groups attached to the graphene edges of GO2, which leads to a higher surface charge density than GO1 flakes. The presence of GO in larger interplanar spaces is confirmed by the decrease in the intensity ratio of the first two XRD peaks, relative to the simulated intensities. This suggests that GO occupies these spaces, as the decrease in intensity is proportional to the GO content (see Figure 3).

For the cobalt and nickel systems (though less evident for the zinc system), the XRD patterns show a decrease in peak broadness as the GO concentration in the MOF

synthesis medium increases. This indicates a larger crystal size (less reduction in crystal size compared to the simulated MOF) as the GO concentration increases. Thus, GO presence seems to favor MOF crystallization, likely due to favorable interactions between the defects in GO and the metal-linker SBUs, which enhance the nucleation and growth processes. This is likely facilitated by the similar phenolate and carboxylate groups found in both ionized GO and the linker. Therefore, our results demonstrate that the crystal structure can be tuned by selecting the nature and loading of the graphene oxide. To minimize the GO content in the solid and reduce the associated synthesis costs, we will continue the CO2 capture and conversion study with the most diluted MOF-GO samples, MOF-GO1 (3 wt%) and MOF-GO2 (3 wt%), in comparison to the bulk MOF.

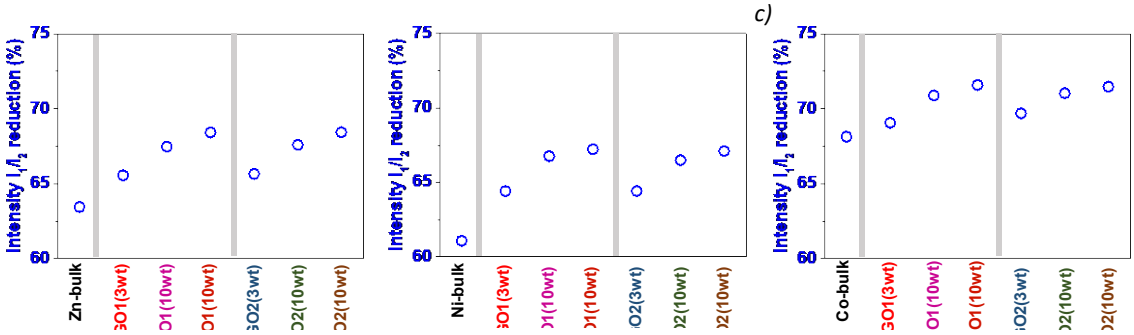


**Figure 3.** Influence of the type of both, graphene oxides and metal on the relative intensity ($I_1/I_2$) decrease of the first two XRD peaks of the MOF-GO samples with respect to the simulated MOFs. GO1 (graphitized), GO2 (non-graphitized).

SEM images are collected in Figure 4, being consistent with those obtained by XRD measurements and agree with previous results.[23] Thus, Zn-bulk particles are larger and better crystallized than those of Ni and Co indicating a similar trend in crystal size, increasing from the nickel-based aggregated nanocrystalline systems with broad XRD peaks to the large isolated zinc-based systems crystals, in line with their sharp XRD

peaks. It is worth mentioning the significant differences (in size and morphology) between the large (in the range of micrometers) isolated and more perfect crystals obtained for the Zn-based GO-MOFs, and the smaller (<100 nm), aggregated and less perfect crystals in the case of Ni/Co-based GO-MOFs, as observed for the bulk MOFs. On the one hand, the metal employed affects the crystal size, with the Zn being the best suited for MOF crystallization and Ni or Co resulting in very small poorly crystallized nanoparticles. Besides, the presence of GO slightly affects the particle size and morphology of the MOF crystals. For example, less defined facets and edges are observed for the larger Zn-MOF-74 crystals in the presence of GO (compare top images in Figure 4). This suggests that the presence of GO in the aqueous solution negatively affects the self-assembly and crystallization of the MOF by incorporation of GO within the metal-organic framework, as supported by the reduced $N_2$-physisorption, see below, associated with the plugging of the MOF pores by GO.

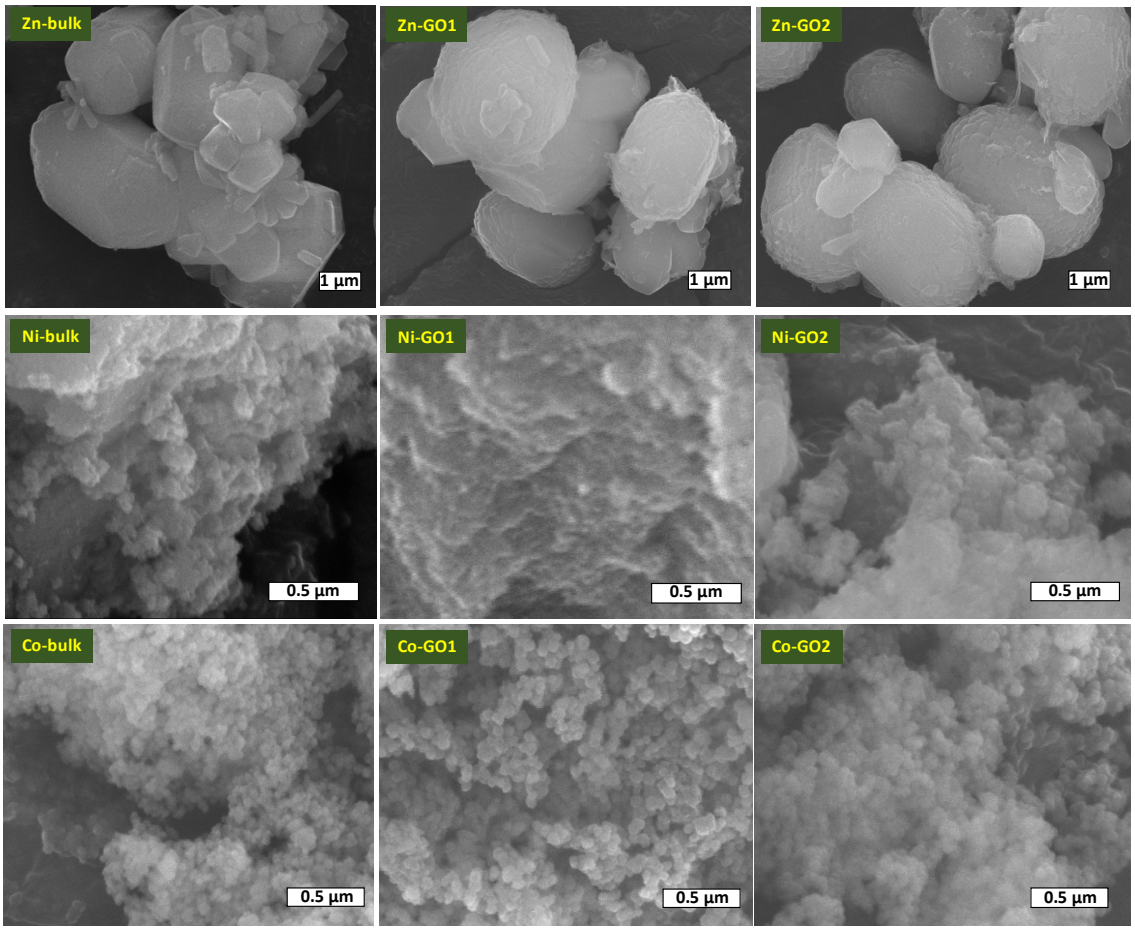


**Figure 4.** SEM images of M=Zn (top), M=Ni (middle) and M=Co (bottom) GO-MOF-based systems, either in the absence, named as M-bulk (left) or presence of M-GO1 (middle) and M-GO2 (right). GO1 (graphitized), GO2 (non-graphitized).

$N_2$ physisorption on the samples indicates a higher porosity for the bulk MOFs, independently of the metal employed (Figure 5), achieving BET surface areas of 278, 237, and 106 $m^2 \cdot g^{-1}$; pore volumes of 0.31, 0.07 and 0.05 $cm^3 \cdot g^{-1}$; and pore sizes of 4, 7 and 21 nm, for Zn, Ni and Co-bulk MOFs, respectively (see Table S3). The hysteresis (in the $P/P_0$=0.3-0.9 range) found in Zn-bulk suggests the presence of a mesoporous structure within the framework, in addition to the well-known microporous MOF-74 crystalline structure (probably achieving a hierarchical meso- and micro-porous structure). This aligns with the isolated nature of the large MOF crystals, which exhibit fused

nanocrystalline domains as observed in the SEM images. These domains are unable to generate interparticle mesoporosity. In contrast, Ni and Co MOFs exhibit hysteresis at higher relative pressures of $P/P_0$ = 0.5-0.9 and $P/P_0 > 0.9$, respectively, indicating the presence of interparticle mesoporosity formed by such small and aggregated nanocrystals. In all cases, the presence of GO within the MOF phase decreases the porosity (especially the microporosity) with respect to the bulk MOF, with a higher decrease for the Zn-systems (from 278 to 21-40 $m^2 \cdot g^{-1}$) with respect to the Ni (from 237 to 185-224 $m^2 \cdot g^{-1}$) and Co (from 106 to 50 $m^2 \cdot g^{-1}$). Interestingly, the smaller size of the Ni-MOF system (ca. 10 nm) is the one less affected (in terms of porosity) by the presence of GO, in contrast to the largest Zn-based nanoparticles (ca. 60 nm), which significantly decreases their porosity probably due to a higher pore blocking by GO.

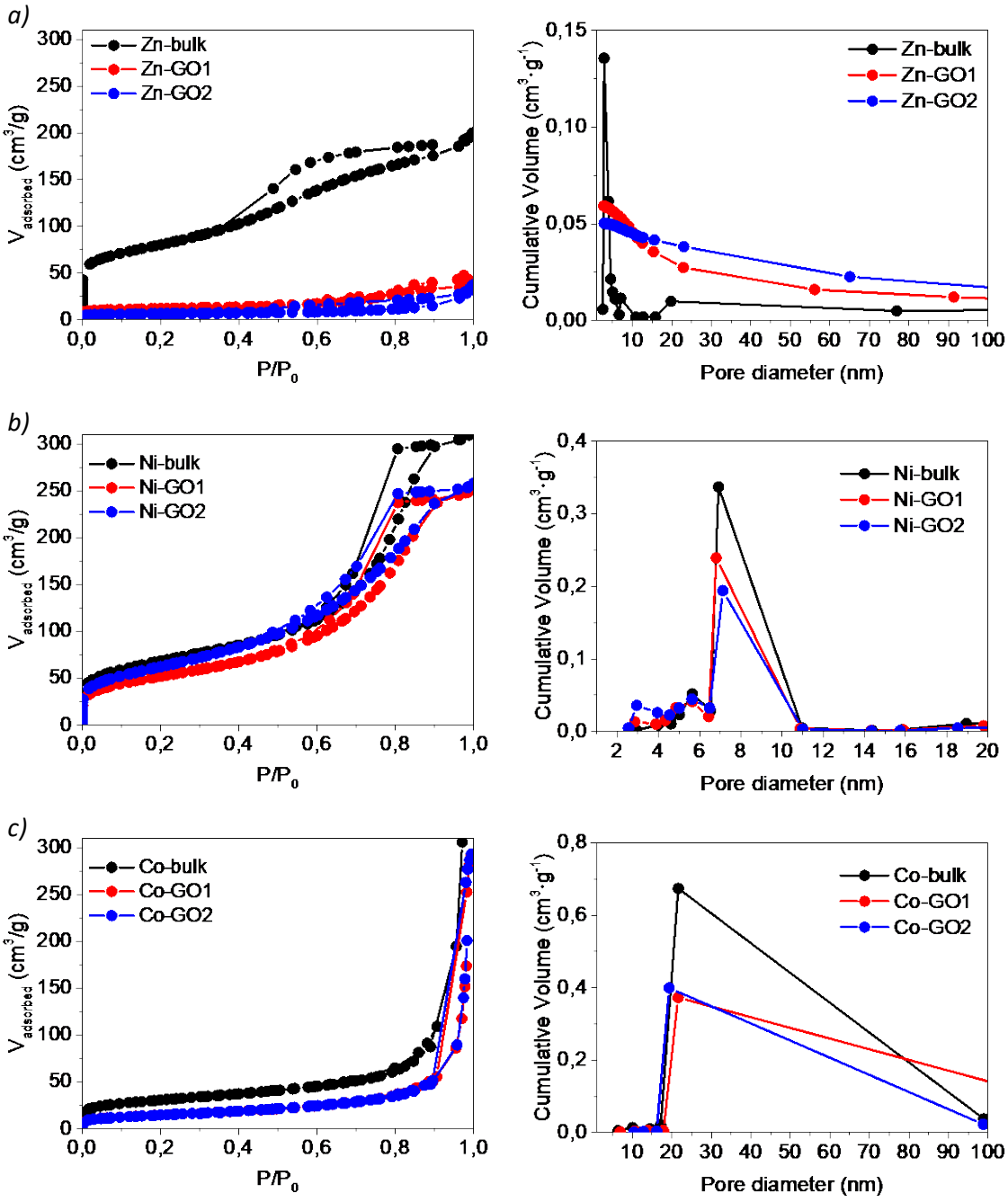


**Figure 5.** $N_2$ isotherms (at -196 ºC) of Zn (a) Ni (b) and Co (c) MOF and GO-MOFs activated at 100 ºC. GO1 (graphitized), GO2 (non-graphitized).

In contrast to $N_2$ physisorption, the $CO_2$ physisorption results indicate a better performance of MOF-GO2 (for all three metals) in terms of the amount of $CO_2$ uptake calculated from the interaction with the y-axis in the Dubinin-Radushkevich plot (see Figure 6 and Table S3), with the Co-based system exhibiting the highest uptake (ca. 5.2

mmol·g$^{-1}$) followed by the Ni-based system (ca. 3.1 mmol·g$^{-1}$) and the Zn-based ones (ca. 3.0 mmol·g$^{-1}$). This trend was previously reported for the three metals employed in the form of bulk MOFs (in the absence of any GO additive).[8] Benchmark Co-GO2 shows the highest $CO_2$ uptake (5.2 mmol·g$^{-1}$) in line with reported $CO_2$ uptakes for Ni and Co-MOF-74 systems.[7] Thus, the GO prepared from non-graphitized carbon nanofibers (GO2) resulted in a higher $CO_2$ uptake than GO-MOFs obtained with graphitized carbon nanofibers (GO1). Using the same Dubinin-Radushkevich plot, $CO_2$ adsorption energies (Ea) were calculated for all the GO MOF samples, which exhibit a different trend to the $CO_2$ uptake, increasing in the order: Zn (ca. 20 kJ·mol$^{-1}$) < Co (ca. 22 kJ·mol$^{-1}$) < Ni (ca. 25 kJ·mol$^{-1}$), all of them in the physisorption range (< 40 kJ mol$^{-1}$). Those values are lower than those previously reported for solvothermal prepared MOFs (ca. 40 kJ·mol$^{-1}$) but also with the Ni-MOF-74 exhibiting higher adsorption energy than the Co-MOF-74, a similar tendency as previously reported for bulk MOF systems prepared under solvothermal conditions and in the absence of GO.[6] As we will demonstrate, the type and amount of GO, along with the MOF crystallite size and its number of defects, are crucial factors in $CO_2$ adsorption. Higher values of $CO_2$ uptake are observed for the Co and Ni systems compared to the Zn systems.

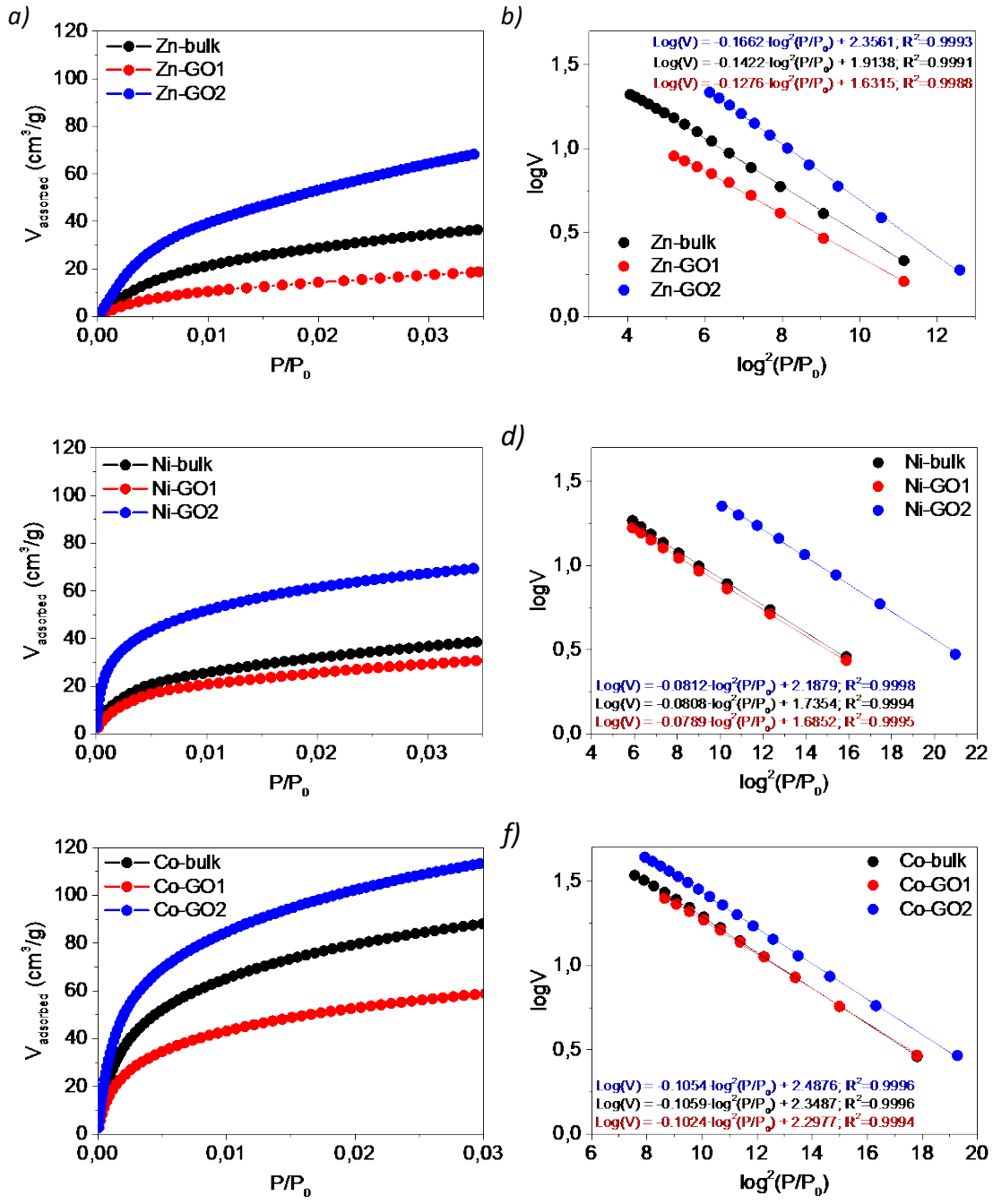


**Figure 6.** (left part) $CO_2$ adsorption isotherms (at 0 ºC) of the Zn (a) Ni (c) and Co (e) MOF (M-bulk and M-GO1/2) activated at 150ºC. (right part) Dubinin-Radushkevich plot (b, d, f) for the calculation of the $CO_2$ adsorption energy ($E_a$) and micropore volume (V). GO1 (graphitized), GO2 (non-graphitized).

Previously we indicated the variations in the MOF structure upon crystallization in the different GO suspensions due to the XRD peak intensity decrease and peak broadness increase. This suggests the interaction of GO layers with the MOF at atomic and nanometric scales, respectively (see Figure 2, Figure 3 and Figure S8). A higher $CO_2$ uptake is found for samples with lower XRD peak intensity (with respect to the simulated MOF), indicating that the presence of GO within the MOF interplanar distances favors $CO_2$ adsorption (see Figure S9). Moreover, MOF-GO composites with smaller crystallite sizes show stronger interactions with $CO_2$ (see Figure 7a for the direct trend between $CO_2$ adsorption energy and crystallite size reduction with respect to the simulated MOF). Indeed, smaller crystallite sizes favor $CO_2$ diffusion into the interlayer galleries of GO with $CO_2$-phylic oxygen groups or to the coordinatively unsaturated metal sites from the MOF inorganic cornerstones, which can be hindered or blocked for larger MOF-GO particle sizes. However, in the MOF-GO1 composites (as opposed to MOF-GO2), $CO_2$ adsorption capacity is lower than the mass-averaged capacity of the constituents. These observations align with the Raman analysis, where C-O intensity and O-C-O downshift suggest increased $CO_2$ uptake (Figure 10), and the G-band shift in Ni hybrids probably points to some MOF influence on GO stacking, enhancing $CO_2$ interaction (Figure S11).

Hybridizing MOFs with GO2 in a 3 wt% amount can enhance $CO_2$ adsorption at low pressures, showing between 1.3 and 1.9-fold $CO_2$ uptake increase with respect to bulk MOFs. Since in GO2 the predominant defects are $sp^3$ (as confirmed in the Raman spectra of the GO-based hybrids), this material presents more O groups than GO1 in which the MOF building blocks could be anchored, favoring the nucleation and growth of the crystal as confirmed by the XRD results. The higher incorporation of MOF in the GO2-based hybrid introduces more porosity and increases the specific surface area resulting in a

higher absorption of $CO_2$. The size of the stronger adsorption region, influenced by the MOF's nature, significantly impacts $CO_2$ adsorption capacity. However, excessive GO will reduce the material's surface area, decreasing $CO_2$ capture performance.

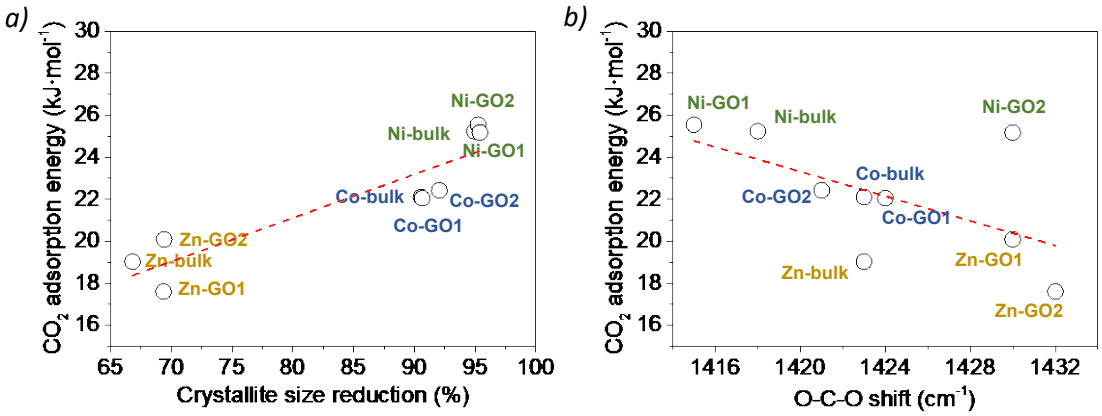


**Figure 7.** $CO_2$ adsorption energy (Ea) dependence on crystallite size (a) or Raman O-C-O shift (b). GO1 (graphitized), GO2 (non-graphitized).

It is worth mentioning the inverse trend between BET surface area and crystal size for the GO-MOF samples (see Figure 8a), indicating the key contribution of external surface area, especially for small (and aggregated) nanoparticles (being inversely proportional to the square of the nanoparticle size, as shown in Figure 8b), only deviating the tendency in the case of the Zn-bulk sample. For this sample, a higher number of crystalline framework micro- and meso-porosity instead of inter-nanoparticle mesoporosity is found, accounting for the high BET surface area independent of its large crystal size (see Figure 4). An apparent trend between pore volume (from the $N_2$ physisorption isotherm) and volume of $CO_2$ uptake (from the $CO_2$ physisorption isotherm) is suggested in Figure 7c, increasing in the order: Zn>Ni>Co. As indicated previously, for each family of materials (Zn, Ni or Co) with similar pore volume values, those being growth in the presence of GO2 exhibit a higher amount of $CO_2$ uptake (see Figures 8c and d). However, no clear trend between crystal size and $CO_2$ adsorption was found. This is probably due to the

higher $CO_2$ uptake with cobalt MOFs, despite the lower crystal size of the nickel MOFs (see Figure 8d), highlighting the importance of other factors besides size and porosity in the uptake of $CO_2$.

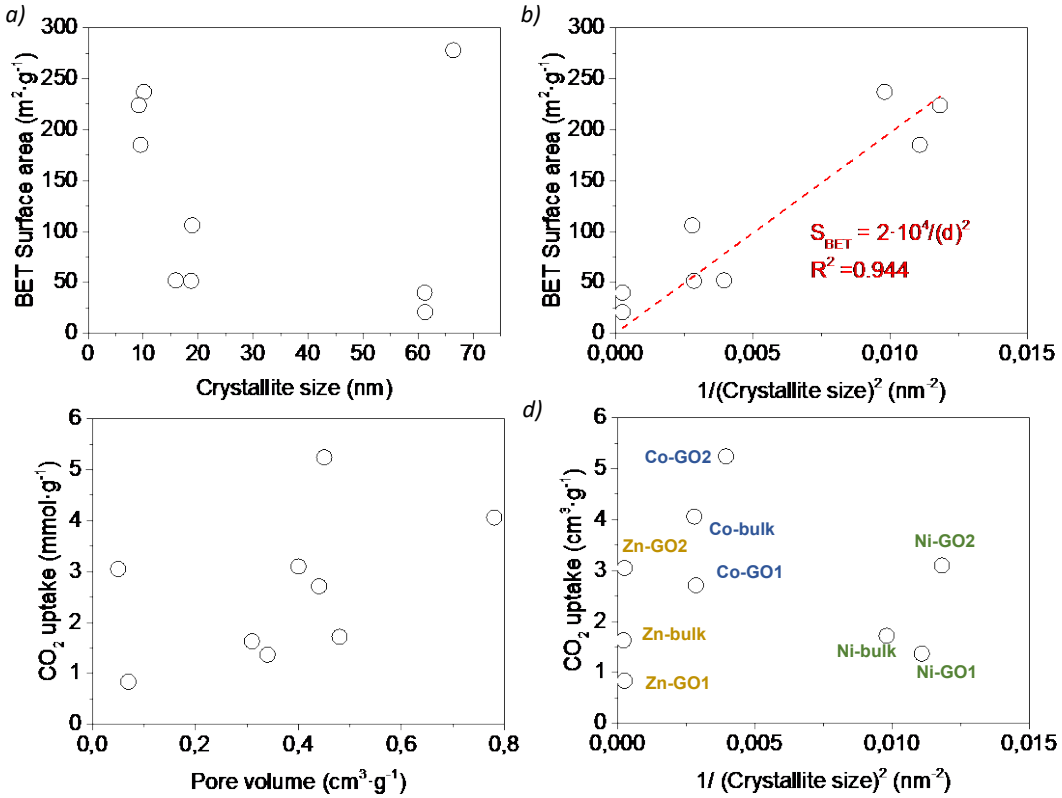


**Figure 8.** BET surface area inverse dependence on crystallite size (a) or linear dependence on their inversed squared (b). Note that Zn-bulk is omitted in the fitting of part b. $CO_2$ uptake dependence on pore volume (c) or on the squared inverse of crystal size (d). GO1 (graphitized), GO2 (non-graphitized).

The sample composition was studied by TGA (Figure S12) and XPS measurements (Tables S4-S9). The bulk metal content was calculated from the TGA results, resulting in a mean value of ca. 40 wt% of metal oxide present in the sample (see specific values in Table S9). This value does not vary to an appreciable amount in the presence or absence of GO and was employed to normalize the catalytic activity of the samples when tested

in the $CO_2$ cycloaddition to epoxides. However, a slight increase in metal content was observed for the Ni and Co-containing samples in the presence of the GO, indicating that the presence of GO in the aqueous suspension favors the MOF growth with respect to the use of pure water. XPS analysis of the surface of the MOF-GO composite suggests a similar direct relation between metal content and GO in the Co and Ni systems, but not for the Zn-MOF-74 sample (see specific values in Table S9).

XPS analysis of the MOFs indicates a similar metal content trend (at the surface) to that determined by TGA (for bulk materials), with the Zn-MOF-74 the one with higher metal proportion (ca. 16% atomic Zn) compared to Ni-MOF-74 and Co-MOF-74 (ca. 9-12% atomic Ni or Co). XPS analysis of metal, oxygen, and carbon signals from the three MOFs either in bulk or in the form of MOF-GO composites was performed to study the effect of the GO on the metal, carbon, and oxygen coordination environment (see Figures S13-S15). On the one hand, the binding energy (BE) of the 2p electrons in the metal (all of them in oxidation state 2) increases from cobalt (780-805 eV) to nickel (ca. 855-885 eV) and then to zinc (1020-1040 eV), in line with their electronegativity. The binding energy of the 2p3 electrons of the metal increases from Co to Zn, in line with the size of the metal ions. Indeed, the radii of $M^{2+}$ ions present in the $MO_6$ octahedral SBUs of the MOF are 0.65 Å, 0.69Å, and 0.74Å, for $Co^{2+}$, $Ni^{2+}$, and $Zn^{2+}$, respectively.[25].

The oxygen 1S signal in the XPS spectra reveals a notable difference in the distribution of the signal for the different MOFs (Figure S14). Specifically, Ni-MOF-74 and Co-MOF-74 show a larger shoulder at 535 eV, accounting for approximately 7% of the total O 1S signal, whereas Zn-MOF-74 shows only about 2%. This shoulder is typically associated with free carboxylic acid (or phenol) CO-H groups that are not coordinated with the metal sites, likely due to point defects in the structure.[26] These uncoordinated

groups suggest the presence of undercoordinated metal sites, which are characteristic of Lewis acid sites that can interact with electron-rich molecules, such as $CO_2$. Additionally, the Ni2p3 component at 855.5 eV, observed in the Ni-MOF-74 spectrum, could be attributed to NiO4 defect sites, further supporting the presence of such defects in the structure.[27] These defect sites could play a crucial role in enhancing the material's catalytic properties, especially in applications like $CO_2$ adsorption and conversion.

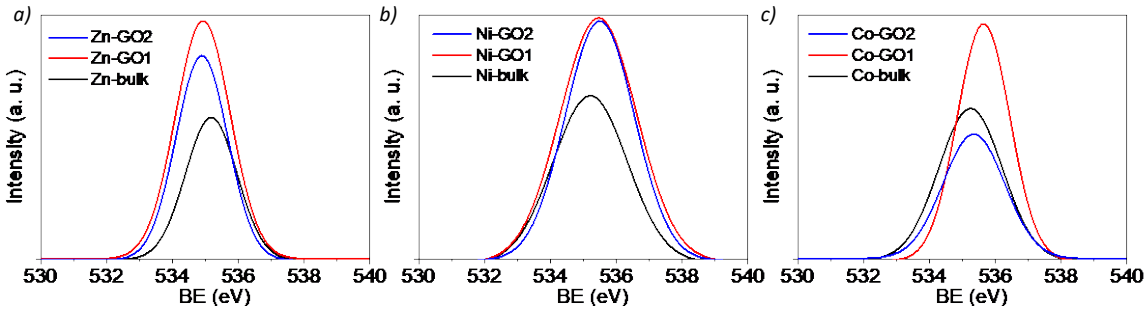


**Figure 9.** XPS (O1s) of Zn (a); Ni (b) and Co (c) MOFs, either in the bulk form (black), or with GO-1 (graphitized, red) and GO-2 (non-graphitized, blue).

Figure 10a illustrates a clear linear relationship between the $CO_2$ adsorption energy and the external surface area of the GO-MOF composites, which is expressed as the square of the inverse of the distance. This plot suggests that smaller MOF nanoparticles provide more surface area and therefore have a higher number of active sites. The active sites are primarily associated with framework defects, particularly the free non-coordinated linkers, which can act as binding sites for $CO_2$. As shown in Figure 10b, these defects increase inversely with the particle size, meaning that smaller nanoparticles (such as those of Co and Ni MOFs) have a higher concentration of these free linkers, which in turn leads to a greater $CO_2$ uptake capacity.

Furthermore, the presence of oxygen-related defects in the framework appears to play a crucial role in $CO_2$ adsorption. Figure 10c demonstrates a direct correlation between the

$CO_2$ adsorption energy and the percentage of the oxygen peak attributed to the free non-coordinating linkers. This strongly suggests that the oxygen defects in the MOF structure are key contributors to the material's ability to capture $CO_2$. Similar findings have been reported for MOF-74, where low-connectivity nodes, which often result in oxygen defects, are identified as significant sites for $CO_2$ adsorption.

Lastly, Figure 10d shows that the $CO_2$ adsorption energy increases with the electronegativity of the defective oxygen atoms. This observation suggests that the oxygen atoms in these defects have a higher ionic character, which can lower the electron density at the adjacent open metal sites. These lower electron densities can enhance the ability of the MOF to interact with $CO_2$ molecules, further increasing the material's $CO_2$ adsorption capacity.[28] This behavior underscores the significance of both metal site reactivity and the framework's oxygen defects in the overall performance of MOF-based systems for $CO_2$ capture.

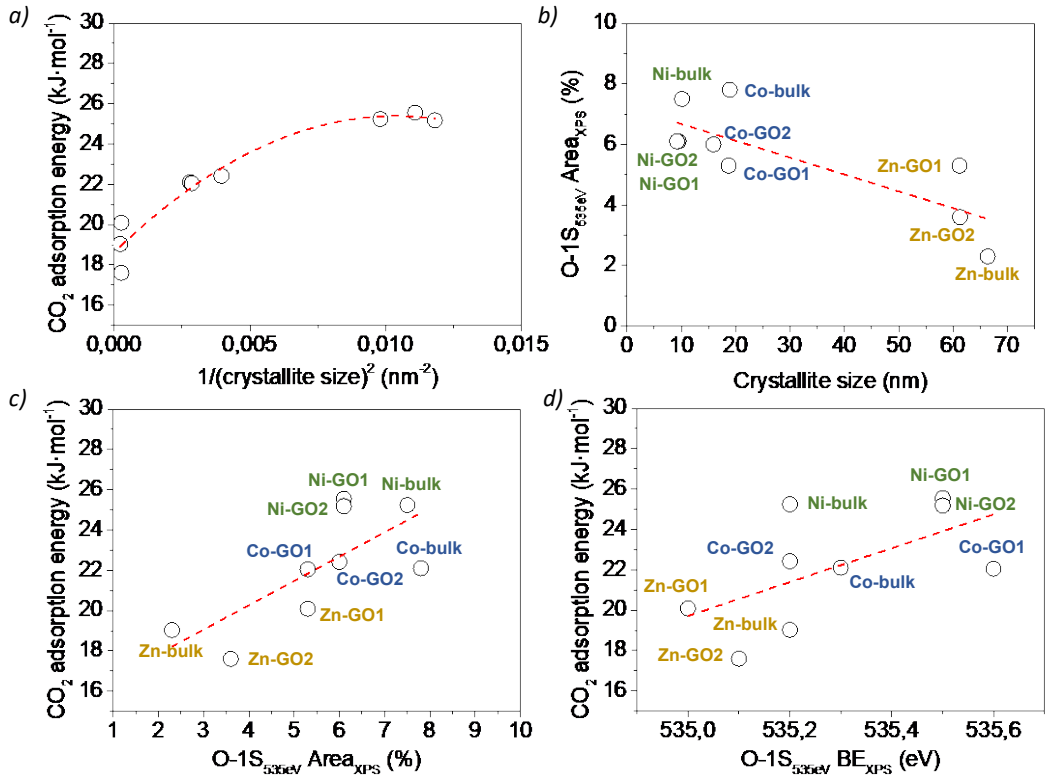


**Figure 10.** $CO_2$ adsorption energy ($E_a$) dependence on crystal size (a), and XPS of the oxygen 1S area at 535 eV (b), (c) or binding energy (d) for the different GO-MOF samples. GO1 (graphitized), GO2 (non-graphitized).

In the case of GO-containing MOFs, the binding energy (BE) trends of the metal 2p electrons follow the order Co-GO < Ni-GO < Zn-GO, with slight differences observed between bulk and GO-containing MOFs. For the Zn systems (Zn-bulk, Zn-GO1, and Zn-GO2), the presence of GO increases the Zn2p3 binding energy (Table S6, Figures S13 a, c), with Zn2p1/2 and Zn2p3/2 peaks shifting from 1045.5 and 1022.4 eV to 1045.7 and 1022.7 eV, respectively. Similarly, for Ni-containing systems, the Ni2p binding energies also increase in GO-containing samples, with peaks at 855.8 eV (Ni2p3A) and 873.3 eV (Ni2p1A) shifting to higher BE (Table S7, Figures S13 b, e, h). Satellite peaks at 860.4 eV (Ni2p3C) and 878.1 eV (Ni2p1C) also shift similarly. However, for Co-containing systems, no clear relationship between BE and GO presence is established (Table S8 and

Figure S14). For bulk Co-MOF, Co2p3 and Co2p1 peaks appear at 781.0 eV and 797.0 eV, respectively, with shifts up to 0.6 eV observed for GO-containing Co-MOF-74, especially in GO2 samples. Overall, the increase in BE for GO-containing MOFs suggests a weakening of electron density at the metal sites, indicating a Lewis acid character that may enhance catalytic performance, particularly in substrate activation.[29, 30]

In the O1s peak, different signals are observed at low and high binding energies for the bulk Zn, Ni, and Co-MOF-74 samples. The low BE signals (530.4/531.9 eV, 530.4/531.6 eV, and 530.7/531.6 eV) are attributed to oxygen coordinated to the metal (e.g., C-O-M), and these signals shift to higher BE in the GO2-containing MOFs.[31] The high BE signals (533.4/535.2 eV, 533.2/535.2 eV, and 533.2/535.3 eV) are related to oxygen in non-coordinated functional groups, such as C=O or carboxylates. Regarding the C1s peak, bulk MOF samples show signals for C-C (284.8 eV) and O-C=O (288.7 eV for Zn, 288.3 eV for Ni, and 288.4 eV for Co). While the C-C signal does not exhibit significant shifts, the O-C=O signal shifts to higher BE upon the addition of GO, especially for the Zn systems, where it increases up to 0.5 eV for GO2. This shift suggests a lower electron density at the carboxylate group of the 2,5-dihydroxyterephthalate linker in the Zn-MOF-74-GO composites (Zn-GO1 and Zn-GO2).

At this point, we wanted to study the chemical reactivity of the samples prepared and characterized towards relevant substrates such as $CO_2$. For that, we studied the $CO_2$ cycloaddition to epoxides, given the interesting $CO_2$ capture properties of the GO-MOF samples. The synthesis of cyclic carbonates from renewable sources, such as biomass-derived epoxides and $CO_2$, allows for the obtention of bio-based plastics (i.e. polycarbonates) with a lower carbon footprint concerning fossil-based plastics and offers the possibility of recycling and biodegradation.[32] The cycloaddition of $CO_2$ to epoxides

needs catalysts with Lewis acid and Lewis base sites to activate the oxygen of the epoxide at the acid sites and to open the ring by nucleophilic attack of the Lewis base. To facilitate the recovery and recycling of the catalyst, and minimize the contamination of the product, the use of heterogeneous catalysts is desired, especially from the industrial point of view. GO has been employed as a catalyst for the $CO_2$ cycloaddition to epoxides due to the presence of oxygen-containing surface-active groups.[33] However, the low density of this 2D material complicates the handling with respect to powders, such as MOFs.

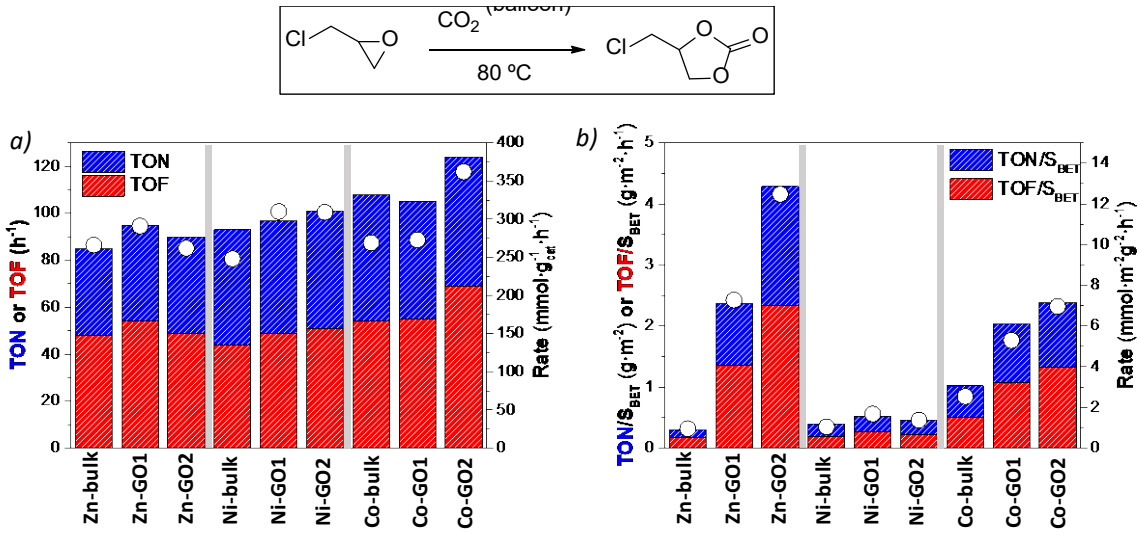


**Figure 11**. (a) $CO_2$ (1 bar, 80ºC) cycloaddition to epichlorohydrin (1.91 mmol) was catalyzed by TBABr (3 mg) and MOF-74 (3 mg) with Zn, Ni, or Co, either as bulk or GO-containing forms. TON (blue bars) was calculated from moles of product per metal site after 3h, TOF (red bars) at 1h, and reaction rate (dots) after 1h. Panel (b) normalizes these results by the BET surface area of each material. GO1 (graphitized), GO2 (non-graphitized).

The performance of the MOF-GO composites was compared with that of bulk MOFs using the solvent-free $CO_2$ cycloaddition to epoxides under 1 bar and 80ºC as a proof-of-concept reaction. (Figure 11). The catalytic activity of the different systems is

proportional to the metal (thermochemical) electronegativity: Co (2.34) > Ni (2.32) > Zn (2.26).[34] This is in line with the direct relation of such parameter and the Lewis acidity of the metal, and the inverse relation of the catalytic activity (and Lewis's acidity or electronegativity) with the ionic radii and BE of the 2p electrons in such metals. However, one cannot neglect the positive effect of the smaller particle size of the Co and Ni systems (with more surface-active sites) on the catalytic activity with respect to the reported Zn system. The effect of GO on the decrease in electron density (BE shift to higher energies) at the surface metal sites further increases the activity of the composite with respect to the bulk MOF (Table S8 and Figure 11a). Moreover, the GO slightly decreases the particle size with respect to the bulk MOF, resulting in more exposed surface-active sites. In the case of the cobalt system, the reaction rate increases to 35% more (and BE increases 0.6 eV) in the MOF-$GO_2$ composite with respect to the bulk MOF. When normalizing the activity of the samples (TON, TOF and rate) to the BET surface area of the samples, clear activity per unit surface boost is observed when the MOF is growth in the presence of GO, especially the one prepared from graphitized carbon fibers (GO2): four times more for the Zn-based systems and twofold for the cobalt-based ones (Figure 11b). Due to the similar BET surface area of the Ni-based systems, no important changes are observed by the presence of GO in the MOF. The catalytic performance dependence on the different physicochemical properties analyzed for each sample is represented in Figures S16-S26, with the most representative relationships summarized in Figure 12.

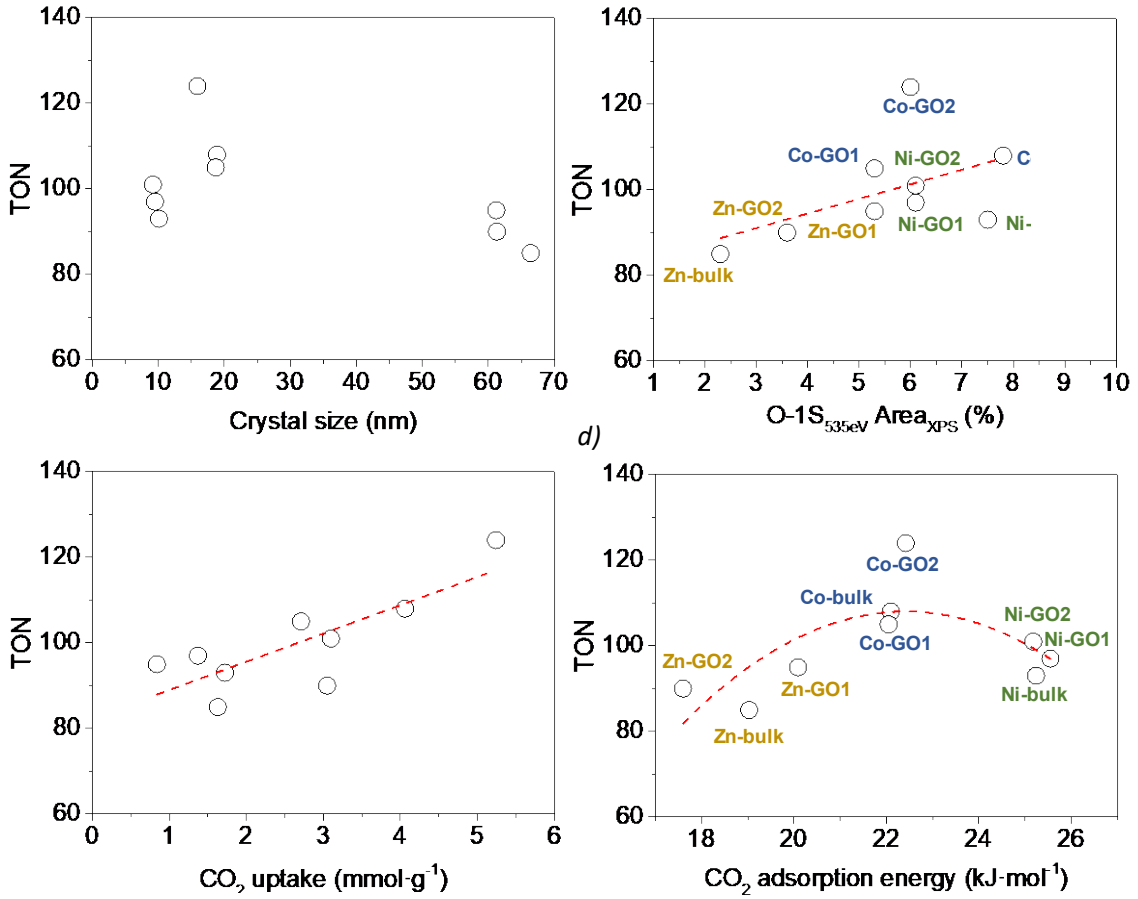


**Figure 12.** TON dependence on crystal size (a), amount of non-bonded MOF linkers (b), $CO_2$ uptake (c) and $CO_2$ adsorption energy (d). GO1 (graphitized), GO2 (non-graphitized).

The crystal size has a key importance in the catalytic activity of the samples since the TON values decrease with the size of the catalyst particles (see Figure 12a). A linear trend is obtained between the catalytic activity (TON), the number of framework defects (see Figure 12b) and $CO_2$ uptake (see Figure 12c). These observations point to such framework defects (e.g. free carboxylic acid, phenol and open metal sites) as the $CO_2$ and epoxide adsorption/catalytic active sites. Finally, a volcano-type plot is obtained when relating the TON to the $CO_2$ adsorption energy (Figure 12d), indicating that Co and Ni MOFs growth in the presence of GO (especially when combining Co and GO2) exhibit the optimal adsorption energies (*ca.* 22-24 kJ·mol$^{-1}$) for a "not-too-strong/not-too-weak"

interaction between the MOF active site and the $CO_2$, optimizing its preconcentration near the defective active sites and its further cycloaddition to the epoxide. The TON value obtained with best-performant Co-GO2 is higher than reported bulk Co-MOF-74 (*ca.* 124 *vs.* 46, respectively) using lower pressure (1 bar *vs.* 20 bar) and temperature (80ºC *vs.* 100ºC).[35] The proposed mechanism for $CO_2$ cycloaddition to epichlorohydrin, as illustrated in Figure S27, suggests that $CO_2$ may be activated at metal centers within the MOF, with defects such as open metal sites and free carboxylic/phenol groups potentially acting as Lewis acids or nucleophiles. Although $CO_2$ adsorption typically occurs in the physisorption region, GO might enhance $CO_2$ activation by modifying the electronic and geometric properties of the MOF. Once the epoxide is activated—either by the metal center or by free carboxylate groups—it could undergo nucleophilic attack by $CO_2$, forming a five-membered ring intermediate (see Figure S).[36] Both basic oxygen groups and undercoordinated metal sites are believed to act as Lewis acid-base pairs, aiding in the activation of $CO_2$ and the epoxide, as well as adsorbing the TBABr co-catalyst.[37] This mechanism could be realized by the defects in both the MOF and GO, potentially improving the overall catalytic performance.

## CONCLUSIONS

The synthesis of MOF-74 with three different metals in pure water and in aqueous solutions of two different graphene oxides allows the tuning of the $CO_2$ sorption properties and its conversion into cyclic carbonates. By using several characterization techniques, XRD, SEM, TGA $N_2$/$CO_2$-physisorption, Raman and XPS, several structure-performance correlations have been found. On the one hand, the metal electrophilicity resulting from a lower electronegativity positively affects its catalytic activity, increasing

in the order: Zn-GO MOFs <Ni-GO MOFs <Co-GO MOFs. On the other hand, the increased $CO_2$ adsorption observed in the hybrids with GO2 can be attributed to the higher number of oxygenated functional groups present in GO2 compared to GO1. These oxygenated groups, such as hydroxyl, epoxy, and carboxyl groups, create additional active sites that facilitate stronger interactions with the MOF, enhancing the material's capacity to adsorb $CO_2$. The presence of these functional groups not only improves the interaction with the MOF but also increases the surface area available for $CO_2$ binding, which contributes to the overall higher adsorption capacity of the GO2-based hybrids. This suggests that GO2, with its higher oxygen content, plays a key role in improving the $CO_2$ uptake performance of the advanced hybrid material interfaces. Smaller MOF crystals enhance $CO_2$ adsorption and catalytic activity by providing more non-coordinated linkers and open metal sites. These increase surface area, improving $CO_2$ binding and facilitating the $CO_2$-epoxide cycloaddition for cyclic carbonate synthesis. The performance of MOF hybrids is also influenced by graphene oxide type, particularly that from graphitized carbon nanofibers, which promotes better interaction with metal centers and provides more active sites. Optimizing pore size, surface area, and metal centers, along with the synergistic effects of graphene oxide, can lead to more efficient and cost-effective $CO_2$ capture and conversion applications.

## ASSOCIATED CONTENT

**Supporting Information**.

The following files are available free of charge.

Additional experimental details, materials, and methods for the MOF-GO synthesis, characterization and catalytic performance (PDF)

AUTHOR INFORMATION

**Corresponding Author**

cirujano@uji.es; mvsal@usal.es, mdm@usal.es

Mercedes ORCID: 0000-0003-2746-8204

**Author Contributions**

The manuscript was written through the contributions of all authors. All authors have given approval to the final version of the manuscript.

ACKNOWLEDGMENT

F. G: C. and N. M. acknowledge the “Ramon y Cajal” contract with code RYC2020-028681-I and RYC2021-033167-I funded MCIN/AEI/10.13039/501100011033 and by "ESF investing in your future", “European Union Next GenerationEU/PRTR”. This work has been partially supported by MICINN-FEDER-AEI 10.13039/501100011033 (PID2021- 124695OB-C22, PID2022-142897OA-I00), MCIN/AEI/10.13039/501100011033 and by the European Union Next Generation EU-PRTR (TED2021-129626B-I00 and TED2021-130288B-I00) and European Regional Development Fund, ERDF, and Junta de Castilla y León (SA106P23). FGC thanks Generalitat Valenciana (CISEJI/2023/78). UJI is acknowledged for the project UJI-2023-03.

REFERENCES

1. Muschi, M.; Serre, C. Progress and challenges of graphene oxide/metal-organic composites. *Coord. Chem. Rev.* **2019**, *387*, 262-272.

2. Jayaramulu, K.; Mukherjee, S.; Morales, D. M.; Dubal, D. P.; Nanjundan, A. K.; Schneemann, A.; Masa, J.; Kment, S.; Schuhmann, W.; Otyepka, M.; Zbořil, R.; Fischer, R. A. Graphene-Based Metal–Organic Framework Hybrids for Applications in Catalysis, Environmental, and Energy Technologies. *Chem. Rev.* **2022**, *122*, 17241−17338.

3. Qu, H. J.; Huang, L. J.; Han, Z. Y.; Wang, Y. X.; Zhang, Z. J.; Wang, Y.; Chang, Q. R.; Wei, N.; Kipper, M. J.; Tang, J. G. A review of graphene-oxide/metal–organic framework composites materials: characteristics, preparation and applications, *J. Porous Mater.* **2021**, *28*, 1837–1865.

4. Kumari, V.; Singh, P. P.; Kaushal, S. Synthesis and applications of metal-organic frameworks and graphene-based composites: A review. *Polyhedron* **2022**, *214*, 115645.

5. Zheng, Y.; Zheng, S.; Xue, H.; Pang, H. Metal-Organic Frameworks/Graphene-Based Materials: Preparations and Applications. *Adv. Funct. Mater.* **2018**, *47*, 1804950.

6. Glover, T. G.; Peterson, G. W.; Schindler, B. J.; Britt, D.; Yaghi, O. MOF-74 building unit has a direct impact on toxic gas adsorption. *Chem. Eng. Sci.* **2011**, *66*, 163-170.

7. Caskey, S. R.; Wong-Foy, A. G.; Matzger, A. J. Dramatic Tuning of Carbon Dioxide Uptake via Metal Substitution in a Coordination Polymer with Cylindrical Pores. *J. Am. Chem. Soc.* **2008**, *130*, 10870–10871.

8. Choe, J. H.; Kim, H.; Hong, C. S. MOF-74 type variants for CO2 capture. *Mater. Chem. Front.* **2021**, *5*, 5172–5185.

9. Tapiador, J.; García-Rojas, E.; López-Patón, P.; Calleja, G.; Orcajo, G.; Martos, C.; Leo, P. Influence of divalent metal ions on CO2 valorization at room temperature by isostructural MOF-74 materials. *J. Env. Chem. Eng.* **2023**, *11*, 109497.

10. Li, W.; Chuah, C. Y.; Yang, Y.; Bae, T.-H. Nanocomposites formed by in situ growth of NiDOBDC nanoparticles on graphene oxide sheets for enhanced CO2 and H2 storage. *Microporous Mesoporous Mater.* **2018**, *265*, 35–42.

11. Konios, D.; Stylianakis, M. M.; Stratakis, E.; Kymakis, E. Dispersion behavior of graphene oxide and reduced graphene oxide, *J. Col. Interf. Sci.* **2014**, *430*, 108-112.

12. Sánchez-Sánchez, M.; Getachew, N.; Díaz, K.; Díaz-García, M.; Chebude, Y.; Díaz, I. Synthesis of metal–organic frameworks in water at room temperature: salts as linker sources. *Green Chem.* **2015**, *17*, 1500-1509.

13. Chen, J.; Yao, B. Li, C.; Shi, G. An improved Hummers method for eco-friendly synthesis of graphene oxide. *Carbon* **2013**, *64*, 225-229.

14. Dubinin, M.M. Adsorption properties and microporous structures of carbonaceous adsorbents. *Carbon* **1987**, *25*, 593-598.

15. Martín-García B, Velázquez MM, Rossella F, Bellani V, Diez E, García Fierro JL, Pérez-Hernández, J. A.; Hernández-Toro, J.; Claramunt, S.; Cirera, A. Functionalization of Reduced Graphite Oxide Sheets with a Zwitterionic Surfactant. *ChemPhysChem*. **2012**, *13*, 3682-90.

16. Lˆ pez-Díaz, D.; Mercedes Vel„zquez, M.; Blanco de La Torre, S.; PÎrez-Pisonero, A.; Trujillano, R.; Fierro, J. L. G.; Claramunt, S.; Cirera, A. The Role of Oxidative Debris on Graphene Oxide Films. *ChemPhysChem* **2013**, *14*, 4002−4009.

17. Hidalgo, R. S.; Lˆ pez-Díaz, D.; Vel„zquez, M. Mercedes Graphene Oxide Thin Films: Influence of Chemical Structure and Deposition Methodology. *Langmuir* **2015**, *31*, 2697−2705.

18. Vera-Agullo, J., Varela-Rizo, H., Conesa, J.A., Almansa, C., Merino, C., Martin-Gullon, I. Evidence for growth mechanism and helixspiral cone structure of stacked-cup carbon nanofibers. *Carbon* **2007**, *45*, 2751-8.

19. Díaz-García, M.; Mayoral, A.; Díaz, I.; Sánchez-Sánchez, M. Nanoscaled M-MOF-74 Materials Prepared at Room Temperature. *Cryst. Growth Des.* **2014**, *14*, 5, 2479–2487.

20. Claramunt, S.; Varea, A.; López-Díaz, D.; Velázquez, M. Mercedes; Cornet, A.; Cirera, A. The Importance of Interbands on the Interpretation of the Raman Spectrum of Graphene Oxide. *J. Phys. Chem. C* **2015**, *119*, 10123–10129.

21. López-Díaz, D.; Delgado-Notario, J. A.; Clericò, V.; Diez, E.; Merchán, M. D.; Velázquez, M. M. Towards Understanding the Raman Spectrum of Graphene Oxide: The Effect of the Chemical Composition. *Coatings* **2020**, *10*, 524.

22. López-Díaz, D.; Holgado, M. L.; García-Fierro, J. L.; Velázquez, M. Mercedes, Evolution of the Raman Spectrum with the Chemical Composition of Graphene Oxide. *J. Phys. Chem. C* **2017**, *121*, 20489–20497.

23. Lopez-Díaz, D.; Merchan, M. D.; Velazquez, M.; Maestro, A. Understanding the Role of Oxidative Debris on the Structure of Graphene Oxide Films at the Air−Water Interface: A Neutron Reflectivity Study. *ACS Appl. Mater. Interfaces* **2020**, *12*, 25453−25463.

24. Flores, J. G.; Díaz-García, M.; Ibarra, I. A.; Aguilar-Pliego, J.; Sánchez-Sánchez, M. Sustainable M-MOF-74 (M = Cu, Co, Zn) prepared in methanol as heterogeneous catalysts in the synthesis of benzaldehyde from styrene oxidation. *J. Solid State Chem.* **2021**, *298*, 122151.

25. Shannon, R. D. Revised Effective Ionic Radii and Systematic Studies of Interatomic Distances in Halides and Chalcogenides. *Acta Crystallographica,* **1976**, *A32*, 751-767.

26. Zou, R-; Li, P.-Z.; Zeng, Y.-F.; Liu, J.; Zhao, R.; Duan, H.; Luo, Z.; Wang, J.-G.; Zou, R.; Zhao, Y. Bimetallic Metal-Organic Frameworks: Probing the Lewis Acid Site for CO2 Conversion. *Small* **2016**, *12*, 2334-2343.

27. Heidary, N.; Chartrand, D.; Guiet, A.; Kornienko, N. Rational incorporation of defects within metal–organic frameworks generates highly active electrocatalytic sites. *Chem. Sci.* **2021**, *12*, 7324–7333.

28. Niu, J.; Li, H.; Tao, L.; Fan, Q.; Liu, W.; Chee-Tan M., Defect Engineering of Low-Coordinated Metal-Organic Frameworks (MOFs) for Improved CO2 Access and Capture. *ACS Appl. Mater. Interfaces* **2023**, *15*, 31664–31674.

29. Huang, C.; Liu, R.; Yang, W.; Li, Y.; Huang, J.; Zhu, H. Enhanced catalytic activity of MnCo-MOF-74 for highly selective aerobic oxidation of substituted toluene. *Inorg. Chem. Front.* **2018**, *5*, 1923–1932.

30. Zha, Q.; Li, M.; Liu, Z.; Ni. Y. Hierarchical Co, Fe-MOF-74/Co/Carbon Cloth Hybrid Electrode: Simple Construction and Enhanced Catalytic Performance in Full Water Splitting. *ACS Sust. Chem. Eng.* **2020**, *8*, 12025-12035.

31. Song, J.-J.; He, B.; Wang, X.; Guo, Y.; Peng, C.; Wang, Y.; Su, Z.; Hao, Q. Hollow porous nanocuboids cobalt-based metal–organic frameworks with coordination defects as anode for enhanced lithium storage. *J Mater Sci* **2021**, *56*, 17178–17190.

32. Rosenboom, J.-G.; Langer, R.; Traverso, G. Bioplastics for a circular economy. *Nature Rev. Mater.* **2022**, 7, 117–137.

33. Zhang, S.; Zhang, H.; Cao, F.; Ma, Y.; Qu, Y. Catalytic Behavior of Graphene Oxides for Converting CO2 into Cyclic Carbonates at One Atmospheric Pressure. *ACS Sustainable Chem. Eng.* **2018**, *6*, 4204–4211.

34. Tantardini, C., Oganov, A.R. Thermochemical electronegativities of the elements. *Nat Commun* **2021**, *12*, 2087.

35. Cho, H.-Y.; Yang, D.-A.; Kim, J.; Jeong, S.-Y.; Ahn, W.-S. CO2 Adsorption and Catalytic Application of Co-MOF-74 Synthesized by Microwave Heating. *Catal. Today* **2012**, 185, 35−40.

36. Sánchez-Velandia, J. E.; Esteve, F.; Maireles, M.; Iglesias, D.; Martín, N.; Zanatta, M.; Sans, V.; Cirujano, F. G.; García-Verdugo, E. One-pot growth of metal-organic frameworks on polymers for catalytic performance enhancement in the CO2 cycloaddition to epoxides. *J. CO2 Util.* **2023**, *78*, 102636.

37. Martín, N.; Maireles, M.; Velandia, J. S.; Altava, B.; Cirujano, F. G.; García-Verdugo, E. Green ionic metal-organic frameworks as nanocatalysts for $CO_2$ fixation. *Nano Research* **2025**, *18*, 94907069.

SYNOPSIS